A&A 397, 405–414 (2003)
DOI: 10.1051/0004-6361:20021567

Astronomy & Astrophysics

Patterns in the weak shear 3-point correlation function

F. Bernardeau[1], L. van Waerbeke[2,3], and Y. Mellier[2,4]

[1] Service de Physique Théorique, CEA/DSM/SPhT, Unité de recherche associée au CNRS, CEA/Saclay, 91191 Gif-sur-Yvette Cedex, France
[2] Institut d'Astrophysique de Paris, 98 bis bd Arago, 75014 Paris, France
[3] Canadian Institute for Theoretical Astrophysics, 60 St George Str., M5S 3H8, Toronto, Canada
[4] LERMA, Observatoire de Paris, 61 avenue de l'Observatoire, 75014 Paris, France

Received 3 January 2002 / Accepted 16 August 2002

Abstract. We explore the scale and angular dependence of the cosmic shear three-point correlation function. The shear field is found to have a much more complex three-point function than the convergence field, but it also exhibits specific motifs which show signatures of gravitational lensing. Exact shear patterns are inferred analytically for some geometrical shear triplets configurations, when simple interpretations can be derived. A more complete description of their geometrical properties is then carried out from ray-tracing numerical simulations and simple models. These patterns reveal typical features that can be utilized for non-Gaussian signal detection in cosmic shear surveys. We test the robustness of these properties against complex noise statistics and non-trivial survey topologies. From these conclusive checks, we predict that the VIRMOS-DESCART survey should allow a detection of a non-Gaussian signal with a comfortable significance for a low matter density Universe.

Key words. cosmology: theory – cosmology: gravitational lensing – cosmology: large-scale structure of Universe

1. Introduction

The detection of cosmic shear signal (van Waerbeke et al. 2000; Bacon et al. 2000; Wittman et al. 2000; Kaiser et al. 2000; Maoli et al. 2001) opened the analysis of large-scale mass distribution in the Universe to weak lensing surveys. As the survey sizes progressively increase, the noise and systematics are reduced to reasonable levels, which permits one to constrain cosmological parameters from the amplitude and the shape of the shear two-point correlation function (Maoli et al. 2001; van Waerbeke et al. 2001b). However, although it is weakly sensitive to the cosmological constant Ω_Λ (Bernardeau et al. 1997), the two-point function is a degenerate combination of the matter density $\Omega_{\rm m}$ of the Universe and the amplitude of the power spectrum σ_8 (Villumsen 1996; Jain & Seljak 1997).

This degeneracy can be broken using the angular dependence of the cosmic shear amplitude (Jain & Seljak 1997), but it relies on the prior knowledge of the shape of the mass power spectrum. An alternative is to directly probe weak shear maps, which contain non-Gaussian features that can be used to derive $\Omega_{\rm m}$ with the only assumption that initial conditions were Gaussian (Bernardeau et al. 1997; van Waerbeke et al. 1999) – this assumption being eventually testable in the data set itself.

So far, all the theoretical predictions regarding non-Gaussian features are based on a critical reconstruction process of either a convergence map (filtered for instance with a top-hat window function) or an aperture mass map (Kaiser et al. 1994; Schneider 1996; Schneider et al. 1998; Bernardeau & Valageas 2000). Unfortunately, the panoramic reconstruction of mass maps from real data turned out to be considerably more difficult than expected. The masking process discussed by van Waerbeke et al. (2000) produces patchy surveys with a non-trivial topology and inhomogeneous noise. The resulting mass maps have poorly understood statistical properties which are practically difficult to handle with confidence. We therefore explore another option that uses direct signatures of Gaussian effects in shear map patterns.

Shear pattern study is a priori somewhat difficult because the third order moment of the local shear vanishes for obvious symmetry reasons. It is therefore necessary to seek peculiar configurations (or geometries) of shear triplets for which a significant signal is expected. This is the aim of this paper. In the next section, we present the exact analytical results obtained for specific geometries, their interpretation and the results obtained from ray-tracing simulations that exhibit the complete three-point function patterns. The detection of these features in these simulations is presented in Sect. 3. These results suggest a detection strategy in cosmic shear surveys that is put forward and tested with mock catalogs in Sect. 4. We checked carefully that the masks do not compromise the possibility of detecting the effect. Finally, we estimate the expected error level of such measurements in the available data sets.

Send offprint requests to: F. Bernardeau,
e-mail: `fbernard@spht.saclay.cea.fr`

2. Theoretical insights

2.1. The local shear statistical properties

In the following we assume that the shear signal is entirely due to cosmic shear effects, and there is no so-called B-mode produced by lens-lens coupling, clustering or any other contamination. Later in the paper (in Sect. 4) we study the impact of residual systematics. This hypothesis naturally leads to the derivation of the shear field $\boldsymbol{\gamma}$ from a potential field that can be written, in Fourier space,

$$\boldsymbol{\gamma}(\boldsymbol{x}) = \int \mathrm{d}^2\boldsymbol{l}\,\kappa_l\,\exp(\mathrm{i}\boldsymbol{l}.\boldsymbol{x})\,\boldsymbol{u}(\theta_l) \tag{1}$$

with

$$\boldsymbol{u}(\theta_l) = \begin{pmatrix}\cos(2\theta_l)\\ \sin(2\theta_l)\end{pmatrix}, \tag{2}$$

where κ_l is the Fourier transform of the local convergence map, the components of $\boldsymbol{l}$ being $l\cos(\theta_l)$ and $l\sin(\theta_l)$. We also assume the validity of the small angle approximation, making the spherical harmonic decomposition unnecessary (Stebbins 1996).

The statistical properties of the variable κ_l can be inferred from those of the projected density contrast. These derivations have been studied in detail in the many papers mentioned in the introduction. Using the small angle approximation (Limber 1954, applied here in Fourier space, Kaiser 1992, 1998; Bernardeau 1995), they give the expression of the convergence power spectrum $P_\kappa(l)$, defined as,

$$\langle\kappa_l\kappa_{l'}\rangle = \delta_{\rm Dirac}(\boldsymbol{l}+\boldsymbol{l}')\,P_\kappa(l) \tag{3}$$

as an integral over the line-of-sight of the 3D matter density contrast power spectrum $P_\delta(k)$,

$$P_\kappa(l) = \int_0^{\chi_{\rm CMB}} \frac{\mathrm{d}\chi}{\mathcal{D}^2}\,w^2(\chi)\,P_\delta\left(\frac{k}{\mathcal{D}}\right) \tag{4}$$

where $w(\chi)$ is the lensing efficiency function (χ is the radial distance, $\mathcal{D}$ is the comoving angular distance). It depends on the cosmological parameters and on the source redshift distribution function, $n(z_{\rm s})$:

$$w(\chi) = \frac{3}{2}\Omega_{\rm m}\int \mathrm{d}z_{\rm s}\,n(z_{\rm s})\frac{\mathcal{D}(\chi_{\rm s}-\chi)\,\mathcal{D}(\chi)}{a\,\mathcal{D}(\chi_{\rm s})} \tag{5}$$

where $\chi_{\rm s}$ is the radial distance to the source plane and when the distances are expressed in units of c/H_0. The phenomenological properties of the convergence field, or similarly the shear field, will be determined by both the shape of the efficiency function and the properties of the cosmic density field.

Likewise, the convergence three-point function can be derived from the cosmic matter three-point function. The small angle approximation can indeed be used again at this level (Bernardeau 1995; Bernardeau et al. 1997), leading to the expression of the $\boldsymbol{l}$-space three point function

$$\langle\kappa_{l_1}\kappa_{l_2}\kappa_{l_3}\rangle = \delta_{\rm Dirac}(\boldsymbol{l}_1+\boldsymbol{l}_2+\boldsymbol{l}_3)\,B_\kappa(\boldsymbol{l}_1,\boldsymbol{l}_2,\boldsymbol{l}_3) \tag{6}$$

with

$$B_\kappa(\boldsymbol{l}_1,\boldsymbol{l}_2,\boldsymbol{l}_3) = \int_0^{\chi_{\rm CMB}} \frac{\mathrm{d}\chi}{\mathcal{D}^2}\,w^3(\chi)\,B_\delta\left(\frac{\boldsymbol{l}_1}{\mathcal{D}},\frac{\boldsymbol{l}_2}{\mathcal{D}},\frac{\boldsymbol{l}_3}{\mathcal{D}}\right) \tag{7}$$

where $B_\delta(\boldsymbol{k}_1,\boldsymbol{k}_2,\boldsymbol{k}_3)$ is the 3D matter density contrast bispectrum:

$$\langle\delta_{\boldsymbol{k}_1}\delta_{\boldsymbol{k}_2}\delta_{\boldsymbol{k}_3}\rangle = \delta_{\rm Dirac}(\boldsymbol{k}1+\boldsymbol{k}_2+\boldsymbol{k}_3)\,B_\delta(\boldsymbol{k}_1,\boldsymbol{k}_2,\boldsymbol{k}_3). \tag{8}$$

The bispectrum B_δ is usually parametrized as follows

$$B_\delta(\boldsymbol{k}_1,\boldsymbol{k}_2,\boldsymbol{k}_3) = Q(\boldsymbol{k}_1,\boldsymbol{k}_2)P_\delta(k_1)P_\delta(k_2) + \mathrm{sym}, \tag{9}$$

where Q is an homogeneous function of the wave vectors $\boldsymbol{k}_1$ and $\boldsymbol{k}_2$. For instance, in the quasi-linear regime it is given by,

$$Q(\boldsymbol{k}_1,\boldsymbol{k}_2) = \frac{10}{7} + \frac{\boldsymbol{k}_1.\boldsymbol{k}_2}{k_1^2} + \frac{\boldsymbol{k}_1.\boldsymbol{k}_2}{k_2^2} + \frac{4}{7}\frac{(\boldsymbol{k}_1.\boldsymbol{k}_2)^2}{k_1^2k_2^2}, \tag{10}$$

whereas in the nonlinear regime Q is often assumed to be a pure number (that depends however on the cosmological models). Several phenomenological models have been proposed to describe the behavior of the three-point matter correlation function, from the quasi-linear regime to the nonlinear regime (the so-called EPT, Colombi et al. 1997 or its extensions with the HEPT, Scoccimarro & Frieman 1999). In particular Scoccimarro & Couchman (2001) have shown that the matter three-point function could be described by,

$$\begin{aligned}Q(\boldsymbol{k}_1,\boldsymbol{k}_2) &= a(k_1,k_2) + b(k_1,k_2)\left(\frac{\boldsymbol{k}_1.\boldsymbol{k}_2}{k_1^2}+\frac{\boldsymbol{k}_1.\boldsymbol{k}_2}{k_2^2}\right)\\ &\quad + c(k_1,k_2)\frac{(\boldsymbol{k}_1.\boldsymbol{k}_2)^2}{k_1^2k_2^2},\end{aligned} \tag{11}$$

where a, b and c depend on scale in a known way.

The properties of the 3D matter three-point function actually extend to the three-point correlation function of the convergence field; e.g. one expects to have

$$B_\kappa(\boldsymbol{l}_1,\boldsymbol{l}_2,\boldsymbol{l}_3) = Q_\kappa(\boldsymbol{l}_1,\boldsymbol{l}_2)P_\kappa(l_1)P_\kappa(l_2) + \mathrm{sym}. \tag{12}$$

To a large extent the functional dependence of the three-point function coefficient Q_κ is left unchanged (Tóth et al. 1989; Bernardeau 1995) although its amplitude is affected by projection effects. This has been investigated in detail at the level of the convergence reduced skewness, which is proportional to the angular averages of $Q_\kappa(\boldsymbol{k}_1,\boldsymbol{k}_2)$[1]. Interestingly the reduced skewness, defined as

$$s_3 = \frac{\langle\kappa^3\rangle}{\langle\kappa^2\rangle^2}, \tag{13}$$

depends on the efficiency function amplitude, and therefore on the cosmological parameter, $\Omega_{\rm m}$, but is less sensitive to the cosmological constant value or the vacuum equation of state (Benabed & Bernardeau 2001). For sources at redshift about unity, calculations give (Bernardeau et al. 1997; Hui 1999; van Waerbeke et al. 2001a),

$$s_3 \sim \Omega_{\rm m}^{-0.8}, \tag{14}$$

---

[1] In the non-linear regime one simply has $s_3 \approx 3\,Q_\kappa$ to a very good approximation.

irrespective of the amplitude of the matter fluctuation[2]. This result also extends to the amplitude of the convergence three-point function so that one expects to have,

$$Q_\kappa \sim \Omega_{\rm m}^{-0.8}. \tag{15}$$

In the following the inter-relation between Q and s_3 will be investigated in more detail. However, it is already obvious that a measurement of Q would be useful to constrain the matter density parameter of the Universe.

2.2. *The shear three-point function*

The general expression of the shear three-point function can be inferred from the $\boldsymbol{l}$-space three point function of the convergence field. However, because $\boldsymbol{\gamma}$ is a 2 component pseudo-vector field there are many possible ways to combine shear triplets. The properties of shear patterns produced by these triplets may be complex. In order to interpret them in a cosmological context it is preferrable to focus first on a few of them that can be easily investigated with analytical calculations. This is the case of $\langle(\boldsymbol{\gamma}(\boldsymbol{x}_1).\boldsymbol{\gamma}(\boldsymbol{x}_2))\,\boldsymbol{\gamma}(\boldsymbol{x}')\rangle$ for a fixed $\boldsymbol{x}_2-\boldsymbol{x}_1$ separation which is a vectorial quantity. This function displays a specific pattern that can be viewed as a 2D vector field.

2.2.1. Computation of $\langle\gamma^2(\boldsymbol{x})\boldsymbol{\gamma}(\boldsymbol{x}')\rangle$

Let start with a simple configuration, when $\boldsymbol{x}_1$ and $\boldsymbol{x}_2$ are pointing in the same location $\boldsymbol{x}$, for which case we have $\boldsymbol{\gamma}(\boldsymbol{x}_1).\boldsymbol{\gamma}(\boldsymbol{x}_2) = \gamma^2(\boldsymbol{x})$. In this case the results make sense only when the filtering effects are taken into account. Otherwise, the result is dominated by the shear behavior at arbitrarily small scales and depends on the detailed behavior of the power spectrum and bi-spectrum in the limit $k \to \infty$, in a regime that might be totally irrelevant for the observations. The shear field is averaged within a smoothing window, but in order to keep a simple notation, we still denote $\boldsymbol{\gamma}(\boldsymbol{x})$ as the smoothed shear vector at the window location $\boldsymbol{x}$. For a top-hat window function of radius θ_0, the three-points function can be written as,

$$\begin{aligned}\langle\gamma^2(\boldsymbol{x})\boldsymbol{\gamma}(\boldsymbol{x}')\rangle = &\int {\rm d}^2\boldsymbol{l}\,{\rm d}^2\boldsymbol{l}'\ W(l\,\theta_0)\ W(|\boldsymbol{l}+\boldsymbol{l}'|\theta_0)\ W(l'\,\theta_0)\ P_\kappa(l)\\ &\times P_\kappa(l')\ Q_\kappa(\boldsymbol{l},\boldsymbol{l}')\left[2\cos(2\theta_{l+l'}-2\theta_{l'})\,e^{{\rm i}\boldsymbol{l}'.(\boldsymbol{x}'-\boldsymbol{x})}\,\boldsymbol{u}(\theta_{l'})\right.\\ &\left.+\cos(2\theta_l-2\theta_{l'})\,e^{{\rm i}(\boldsymbol{l}+\boldsymbol{l}').(\boldsymbol{x}'-\boldsymbol{x})}\,\boldsymbol{u}(\theta_{l'+l})\right]\end{aligned} \tag{16}$$

where W is the $\boldsymbol{l}$-space top-hat window function,

$$W(x) = \frac{J_1(x)}{x}, \tag{17}$$

where $J_1(x)$ is the first Bessel function of the first kind.

The computation of expression (16) is still complicated in general, but it simplifies in the large separation limit, $\theta_0 \ll |\boldsymbol{x}-\boldsymbol{x}'|$. In this case it is possible to express the result in terms of the square root of the variance of the filtered convergence σ_κ and the convergence-shear correlation function $\xi_{\kappa\gamma}$.

In the large separation limit, in the first term of Eq. (16), the values of l' that will most contribute are of the order of $1/|\boldsymbol{x}-\boldsymbol{x}'|$ whereas that of l will be of the order of $1/\theta_0$; in the second term the integrations in l and l' factorize out (in this configuration $W(|\boldsymbol{l}'+\boldsymbol{l}|)$ does not play a role) and both l and l' are of the order of $1/\theta_0$. As a consequence, the first term of (16) is of the order of $\sigma_\kappa^2\,\xi_{\kappa\gamma}$ whereas the second is of the order of $\xi_{\kappa\gamma}^2$ and is thus smaller[3]. Furthermore, as in the first term $l' \ll l$, it is possible to expand all quantities in l'/l,

$$\cos(2\theta_{l+l'}-2\theta_{l'}) \approx 1-\frac{l'^2}{2\,l^2}\sin^2(\theta_l-\theta_{l'})+\dots \tag{18}$$

$$W(|\boldsymbol{l}+\boldsymbol{l}'|\theta_0) \approx W(l\theta_0)+l\theta_0\ W'(l\theta_0)\frac{\boldsymbol{l}.\boldsymbol{l}'}{l^2}+\dots \tag{19}$$

Once a shape for Q_κ is given, computing the integral of the angle of $\boldsymbol{l}$ is straightforward. In general, following the prescription of Scoccimarro & Couchman, Eq. (11), one can write[4]

$$Q_\kappa(\boldsymbol{l},\boldsymbol{l}') = a(l,l')+b(l,l')\left(\frac{\boldsymbol{l}.\boldsymbol{l}'}{l^2}+\frac{\boldsymbol{l}.\boldsymbol{l}'}{l'^2}\right)+c(l,l')\frac{(\boldsymbol{l}.\boldsymbol{l}')^2}{l'^2\,l^2} \tag{20}$$

from which one gets,

$$\begin{aligned}\langle\gamma^2(\boldsymbol{x})\boldsymbol{\gamma}(\boldsymbol{x}')\rangle = 2\pi&\int l{\rm d}l\,{\rm d}^2\boldsymbol{l}'\ P_\kappa(l)\,P_\kappa(l')\,{\rm e}^{{\rm i}\boldsymbol{l}'.(\boldsymbol{x}'-\boldsymbol{x})}\\ &\times\left\{W^2(l\,\theta_0)\,W(l'\,\theta_0)\left[a(l,l')+\frac{c(l,l')}{2}\right]\right.\\ &\left.+\frac{l\theta_0}{2}W(l\theta_0)W'(l\theta_0)W(l'\,\theta_0)b(l,l')\right\}\boldsymbol{u}(\theta_{l'}).\end{aligned} \tag{21}$$

When $a(l,l')$, $b(l,l')$ and $c(l,l')$ are pure numbers as it is the case for the quasi-linear regime, the integrals in l and l' factorize and lead to an expression of the form,

$$\langle\gamma^2(\boldsymbol{x})\boldsymbol{\gamma}(\boldsymbol{x}')\rangle = c_{2\,1}\sigma_\kappa^2\int{\rm d}^2\boldsymbol{l}'P_\kappa(l')W(l'\theta_0)\,{\rm e}^{{\rm i}\boldsymbol{l}'.(\boldsymbol{x}'-\boldsymbol{x})}\,\boldsymbol{u}(\theta_{l'}) \tag{22}$$

where $c_{2\,1}$ is a pure number. It can actually be noted that $c_{2\,1}$ identifies with the coefficient appearing in the expression of the reduce joint cumulant,

$$\langle\kappa^2(\boldsymbol{x})\kappa(\boldsymbol{x}')\rangle = c_{2\,1}\,\sigma_\kappa^2\,\langle\kappa(\boldsymbol{x})\kappa(\boldsymbol{x}')\rangle \tag{23}$$

in the large separation limit (Bernardeau 1996). It has actually been already computed in Bernardeau et al. (1997) in the quasi-linear regime. It scales as $\Omega_{\rm m}^{-0.8}$ and it is mainly independent of the spectrum index.

The last integral in (22) is equal to the convergence-shear correlation function,

$$\boldsymbol{\xi}_{\kappa\gamma}(\boldsymbol{x}') \equiv \int{\rm d}^2\boldsymbol{l}'P_\kappa(l')W(l'\theta_0)\,{\rm e}^{{\rm i}\boldsymbol{l}'.\boldsymbol{x}'}\,\boldsymbol{u}(\theta_{l'}), \tag{24}$$

and can be computed by noticing that

$$\begin{aligned}&\int{\rm d}^2\boldsymbol{l}'P_\kappa(l')W(l'\theta_0)\,e^{{\rm i}\boldsymbol{l}'.(\boldsymbol{x}'-\boldsymbol{x})}\,\boldsymbol{u}(\theta_{l'}) =\\ &-\begin{pmatrix}\partial^2_{x'}-\partial^2_{y'}\\ 2\partial_{x'}\partial_{y'}\end{pmatrix}\int\frac{{\rm d}^2\boldsymbol{l}'}{l'^2}P_\kappa(l')W(l'\theta_0)\,{\rm e}^{{\rm i}\boldsymbol{l}'.(\boldsymbol{x}'-\boldsymbol{x})}.\end{aligned} \tag{25}$$

---

[2] The reduced skewness can however depend on the normalization of the matter density fluctuations in the intermediate regime between the quasi-linear and the nonlinear regime.

[3] This is a very general scheme for such computations. It is described in more details in Bernardeau et al. (2001).

[4] The coefficients a, b and c that appear in Eqs. (11) and (20) are not necessarily identical because of the projection effects.

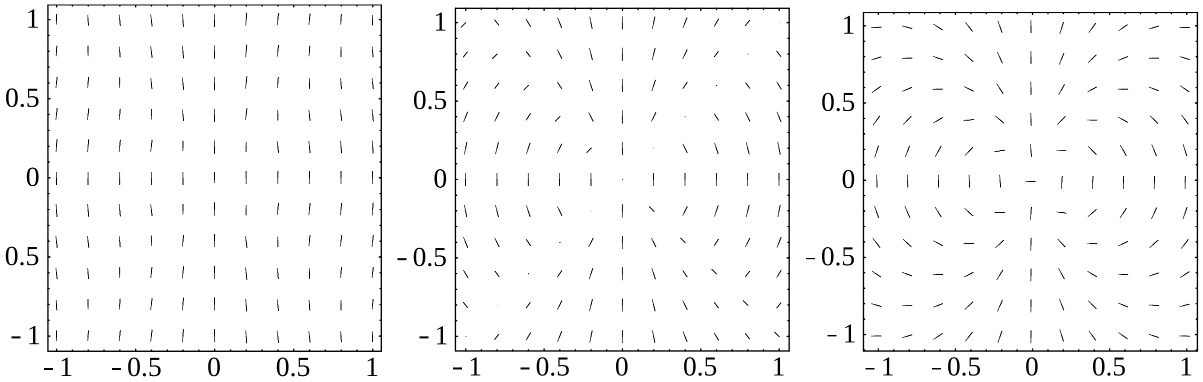

Fig. 1. Shear patterns in the vicinity of one of the pair points either $\boldsymbol{x}_1$ or $\boldsymbol{x}_2$ (positioned at the center of the plot) for $n = -1.5$, $n = -1$ and $n = -0.5$ (from left to right) as a function of $\boldsymbol{x}'$. It illustrates the results of Eq. (35). Coordinates are arbitrary.

So, if one defines ξ_ϕ as the potential two-point correlation function,

$$\begin{aligned}\xi_\phi(x) &= \int \frac{\mathrm{d}^2\boldsymbol{l}'}{l'^2} P_\kappa(l') W(l'\theta_0)\,\mathrm{e}^{\mathrm{i}\boldsymbol{l}'.\boldsymbol{x}} \\ &= 2\pi \int \frac{\mathrm{d}l'}{l'} P_\kappa(l') W(l'\theta_0)\, J_0(l'\,x), \end{aligned} \tag{26}$$

we get

$$\int \mathrm{d}^2\boldsymbol{l}' P_\kappa(l') W(l'\theta_0)\,\mathrm{e}^{\mathrm{i}\boldsymbol{l}'.\boldsymbol{x}'}\,\boldsymbol{u}(\theta_{l'}) = -\begin{pmatrix} x'^2 - y'^2 \\ 2\,x'\,y' \end{pmatrix} \left[\frac{1}{|\boldsymbol{x}'|^2}\xi''_\phi(|\boldsymbol{x}'|) - \frac{1}{|\boldsymbol{x}'|^3}\xi'_\phi(|\boldsymbol{x}'|)\right]. \tag{27}$$

Therefore, in the case of a power law spectrum, $P(l) \sim l^n$, one has for $x \gg \theta_0$

$$\xi_\phi(x) \sim x^{-n} \tag{28}$$

so that

$$\left[\xi''_\phi(|\boldsymbol{x}'|) - \frac{1}{|\boldsymbol{x}'|}\xi'_\phi(|\boldsymbol{x}'|)\right] = n(n+2)\frac{\xi_\phi(|\boldsymbol{x}'|)}{|\boldsymbol{x}'|^2} \tag{29}$$

which is equal to $-(n+2)/n\;\xi_\kappa(|\boldsymbol{x}'|)$. Hence, the 3-point function clearly depends on the slope of the power spectrum:

$$\langle\gamma^2(\boldsymbol{x})\boldsymbol{\gamma}(\boldsymbol{x}')\rangle = -\frac{n+2}{n}\,c_{2\,1}\,\sigma_\kappa^2\,\xi_\kappa(|\boldsymbol{d}'|)\begin{pmatrix}\cos(2\theta_{d'}) \\ \sin(2\theta_{d'})\end{pmatrix}, \tag{30}$$

where $\boldsymbol{d}'$ is the distance vector between $\boldsymbol{x}'$ and $\boldsymbol{x}$, $\boldsymbol{d}' = \boldsymbol{x}' - \boldsymbol{x}$, and $\theta_{d'}$ is its angle to the first axis. It is interesting to notice that, contrary to the convergence field, the amplitude of the three-point shear function vanishes (in units of the square of the two-point function) when $n \to -2$. Although this result is obtained in some specific limiting configuration it expresses a general trend: when n is close to -2 the shear is dominated by very long wavelength[5], much longer than $\boldsymbol{x}' - \boldsymbol{x}$, so that what is computed here is the same as contracted three point functions that all vanish for symmetry reasons.

For $n \approx -1.5$ and sources at redshift unity, we know from Bernardeau et al. (1997) that in the quasilinear regime,

$$c_{2\,1} \approx 36.7/\Omega_{\mathrm{m}}^{0.8}, \tag{31}$$

a result that can be obtained from Eq. (21) with $a = 10/7$, $b = 1$, $c = 4/7$. Consequently, observables like $\langle\gamma^2(\boldsymbol{x})\boldsymbol{\gamma}(\boldsymbol{x}')\rangle / \left(\sigma_\kappa^2\,\xi_\kappa(|\boldsymbol{x}'|)\right)$ would provide alternative ways for measuring the cosmic density parameter Ω_{m}. They do not require mass reconstruction but still require some filtering which, for the reasons mentioned in the beginning, we would like to avoid.

2.2.2. Computation of $\langle(\boldsymbol{\gamma}(\boldsymbol{x}_1).\boldsymbol{\gamma}(\boldsymbol{x}_2))\,\boldsymbol{\gamma}(\boldsymbol{x}')\rangle$

In the previous paragraph the calculations were tractable without a strong hypothesis about the shape of the bispectrum. Here, we explore more generic geometrical cases, so more specific assumptions about the bispectrum are necessary to carry out analytical computations. We assume it follows the prescription usually adopted in the strongly non-linear regime, that is, the coefficient Q_κ introduced in Eq. (12) is constant (but depends on the cosmological model). We do expect that this is a valid approximation at the scales we are interested in (below 5′) and in any case the results presented in the following do not critically rely on this assumption, as is the case for the skewness of the convergence.

A quantity like $\langle(\boldsymbol{\gamma}(\boldsymbol{x}_1).\boldsymbol{\gamma}(\boldsymbol{x}_2))\;\boldsymbol{\gamma}(\boldsymbol{x}')\rangle$ is expected to behave as $\langle\boldsymbol{\gamma}^2(\boldsymbol{x})\,\boldsymbol{\gamma}(\boldsymbol{x}')\rangle$ when $|\boldsymbol{x}_1 - \boldsymbol{x}_2| \ll |\boldsymbol{x}' - (\boldsymbol{x}_1 + \boldsymbol{x}_2)/2|$. In this limit its expression is given by

$$\begin{aligned}\langle(\boldsymbol{\gamma}(\boldsymbol{x}_1).\boldsymbol{\gamma}(\boldsymbol{x}_2))\;\boldsymbol{\gamma}(\boldsymbol{x}')\rangle &= \int \mathrm{d}^2\boldsymbol{l}\,\mathrm{d}^2\boldsymbol{l}'\;P_\kappa(l)\,P_\kappa(l') \\ &\times Q_\kappa(\boldsymbol{l},\boldsymbol{l}')\,\mathrm{e}^{\mathrm{i}\boldsymbol{l}.(\boldsymbol{x}_2-\boldsymbol{x}_1)+\mathrm{i}\boldsymbol{l}'.(\boldsymbol{x}'-\boldsymbol{x}_1)} \\ &\times \cos(2\theta_{l+l'} - 2\theta_{l'})\,\boldsymbol{u}(\theta_{l'}) + \{\boldsymbol{x}_1 \leftrightarrow \boldsymbol{x}_2\}. \end{aligned} \tag{32}$$

Here the filtering effects can be ignored since all points are taken at finite distance.

In the case of a simple bispectrum – with only a non-zero monopole term and $b = c = 0$ – and with the help of the expansion (18), the integrals over the angle θ_l and $\theta_{l'}$ in (32) can be

---

[5] When $n = -2$ the computation of the variance of κ (or γ) shows a divergence at $l \to 0$ when it is computed with the Limber approximation. It means that in the limit $n \to -2$ the fluctuations of the shear field are dominated by infinitely long wave modes, much longer than $|\boldsymbol{x} - \boldsymbol{x}'|$. Moreover, when $n < -2$ the whole calculation presented here, which is based on the small angle approximation, becomes invalid.

computed explicitly. It leads to an expression of the form

$$\langle(\boldsymbol{\gamma}(\boldsymbol{x}_1).\boldsymbol{\gamma}(\boldsymbol{x}_2))\,\boldsymbol{\gamma}(\boldsymbol{x}')\rangle = c_{21}\xi_\kappa(|\boldsymbol{x}_2-\boldsymbol{x}_1|)\xi_{\kappa\gamma}(|\boldsymbol{d}'|)\begin{pmatrix}\cos(2\theta_{d'})\\ \sin(2\theta_{d'})\end{pmatrix}, \tag{33}$$

where $\boldsymbol{d}' = \boldsymbol{x}' - (\boldsymbol{x}_1 + \boldsymbol{x}_2)/2$. It generalizes the result of Eq. (22).

This result can be simply interpreted: an excess of shear at a given position is most likely associated with a mass overdensity, so that the shear at finite distance from the point pairs is preferentially tangential. This non-zero three point function is therefore simply associated with the usual skewness. It directly comes from the relative excess of overdensity regions compared to low density areas.

The situation becomes more complex when the assumption $|\boldsymbol{x}_1 - \boldsymbol{x}_2| \ll |\boldsymbol{x}' - (\boldsymbol{x}_1 + \boldsymbol{x}_2)/2|$ is dropped. Another restricting case can however be investigated, when $|\boldsymbol{x}' - \boldsymbol{x}_1| \ll |\boldsymbol{x}_1 - \boldsymbol{x}_2|$. In this case the two dominant contributions are

$$\begin{aligned}\langle(\boldsymbol{\gamma}(\boldsymbol{x}_1).\boldsymbol{\gamma}(\boldsymbol{x}_2))\,\boldsymbol{\gamma}(\boldsymbol{x}')\rangle &= \int \mathrm{d}^2\boldsymbol{l}\,\mathrm{d}^2\boldsymbol{l}'\,P_\kappa(l)\,P_\kappa(l')\,Q_\kappa(\boldsymbol{l},\boldsymbol{l}')\\ &\times\Big[\mathrm{e}^{\mathrm{i}\boldsymbol{l}.(\boldsymbol{x}_2-\boldsymbol{x}_1)+\mathrm{i}\boldsymbol{l}'.(\boldsymbol{x}'-\boldsymbol{x}_1)}\cos(2\theta_{\boldsymbol{l}+\boldsymbol{l}'}-2\theta_{\boldsymbol{l}})\,\boldsymbol{u}(\theta_{\boldsymbol{l}'})\\ &+\mathrm{e}^{\mathrm{i}\boldsymbol{l}.(\boldsymbol{x}'-\boldsymbol{x}_1)+\mathrm{i}\boldsymbol{l}'.(\boldsymbol{x}'-\boldsymbol{x}_2)}\cos(2\theta_{\boldsymbol{l}}-2\theta_{\boldsymbol{l}'})\,\boldsymbol{u}(\theta_{\boldsymbol{l}'+\boldsymbol{l}})\Big].\end{aligned} \tag{34}$$

Then similar calculations can be performed, again assuming that the bispectrum simply factorizes in terms of the power spectrum as in the nonlinear regime. It leads to the expressions

$$\begin{aligned}\langle(\boldsymbol{\gamma}(\boldsymbol{x}_1).\boldsymbol{\gamma}(\boldsymbol{x}_2))\,\boldsymbol{\gamma}(\boldsymbol{x}')\rangle &= c_{21}\,\xi_{\kappa\gamma}\,(|\boldsymbol{x}_2-\boldsymbol{x}_1|)\Bigg[\xi_\kappa(|\boldsymbol{x}'-\boldsymbol{x}_1|)\begin{pmatrix}1\\0\end{pmatrix}\\ &+(\xi_{\rm tt}\,(|\boldsymbol{x}'-\boldsymbol{x}_1|)-\xi_{\rm rr}\,(|\boldsymbol{x}'-\boldsymbol{x}_1|))\begin{pmatrix}\cos(4\theta_{\boldsymbol{x}'-\boldsymbol{x}_1})\\ \sin(4\theta_{\boldsymbol{x}'-\boldsymbol{x}_1})\end{pmatrix}\Bigg]\end{aligned} \tag{35}$$

if the $\boldsymbol{x}_2-\boldsymbol{x}_1$ vector is along the first direction. In this expression we have decomposed the shear two-point correlation function into the tangential part $\xi_{\rm tt}$ (i.e. the correlation function of the shear components along the $\boldsymbol{x}_2 - \boldsymbol{x}_1$ direction) and the radial part $\xi_{\rm rr}$. The relative importance of the 2 terms depend on the power spectrum shape, e.g.

$$Q_2 \equiv \frac{\xi_{\rm tt}-\xi_{\rm rr}}{\xi_\kappa} = \frac{(n+2)(n+4)}{(n-2)n}\cdot \tag{36}$$

This shape is actually a direct transcription of the behavior of the shear two-point functions (for a component γ_1 of $\boldsymbol{\gamma}(\boldsymbol{x}_1)$ along a fixed direction),

$$\begin{aligned}\langle\gamma_1(\boldsymbol{x}_1)\,\boldsymbol{\gamma}(\boldsymbol{x}')\rangle &= \Bigg[\xi_\kappa(|\boldsymbol{x}'-\boldsymbol{x}_1|)\begin{pmatrix}1\\0\end{pmatrix}\\ &+(\xi_{\rm tt}(|\boldsymbol{x}'-\boldsymbol{x}_1|)-\xi_{\rm rr}(|\boldsymbol{x}'-\boldsymbol{x}_1|))\begin{pmatrix}\cos(4\theta_{\boldsymbol{x}'-\boldsymbol{x}_1})\\ \sin(4\theta_{\boldsymbol{x}'-\boldsymbol{x}_1})\end{pmatrix}\Bigg]\cdot\end{aligned} \tag{37}$$

Nonetheless these patterns are indicative of the physical effects one might want to look for. The pseudo-vector field structure of the three-point function displays a pattern which corresponds to the superposition of a uniform field and a specific mass-dipole contribution. The relative weight of the two terms depends on the power law index. When n is close to -2, structures are mostly dominated by long-wavelength modes and the shear patterns are aligned (in other words $\xi_{\rm tt}$ and $\xi_{\rm rr}$ are equal). In contrast when n is close to 0, structures are given by the point-mass Poisson distribution (and $\xi_{\rm tt}$ and $\xi_{\rm rr}$ are opposite to each-other).

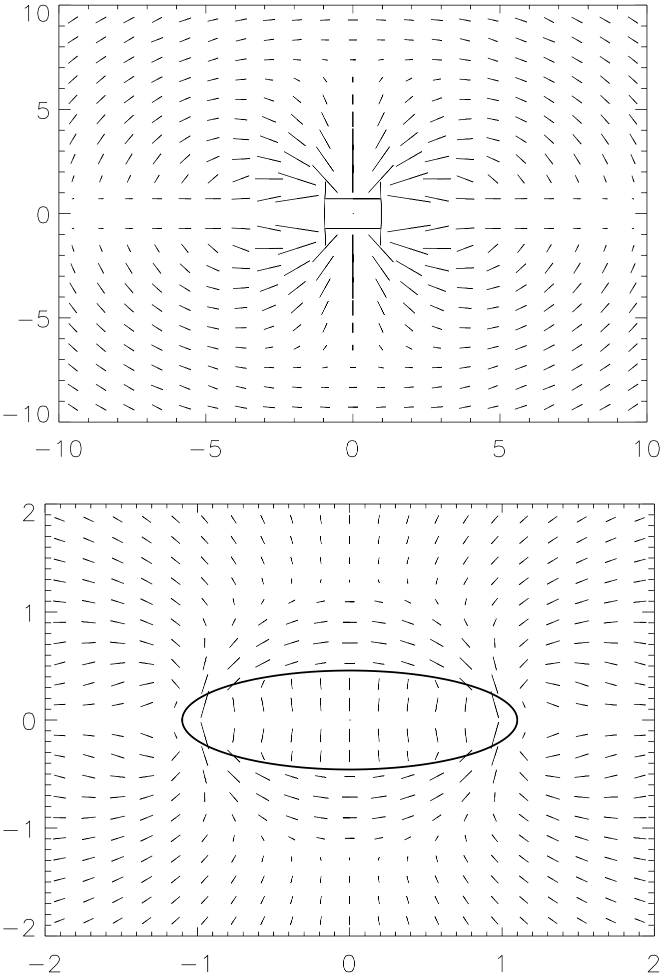

Fig. 2. The shear pattern obtained by a numerical integration in case of a power spectrum index $n = -1$ and for a three-point function that obeys the hierarchical ansatz, Q_κ = constant in Eq. (12). The pair points are at position $(-1,0)$ and $(1,0)$ in both panels. The only difference in the two panels is the scale at which the pattern is drawn.

Plots in Fig. 1 show the shear patterns near pair points for different power law indices. One can see that for $n \leq -1$ the shear pattern around the points is mostly uniform.

2.3. Semi-analytical results

The exact analytical results presented in the previous paragraphs only correspond to simple cases. They provide insightful descriptions of the behavior of the shear three-point function but have a limited practical interest if their exact validity domain is unknown. More general results can be obtained, but only for specific cosmological models through numerical computation and ray-tracing simulations.

Figure 2 shows the shear pattern expected for a power law spectrum of index $n = -1$ and for a matter three-point function shape given by the non-linear regime. The patterns observed around the pair points (located at positions [−1, 0] and [1, 0])

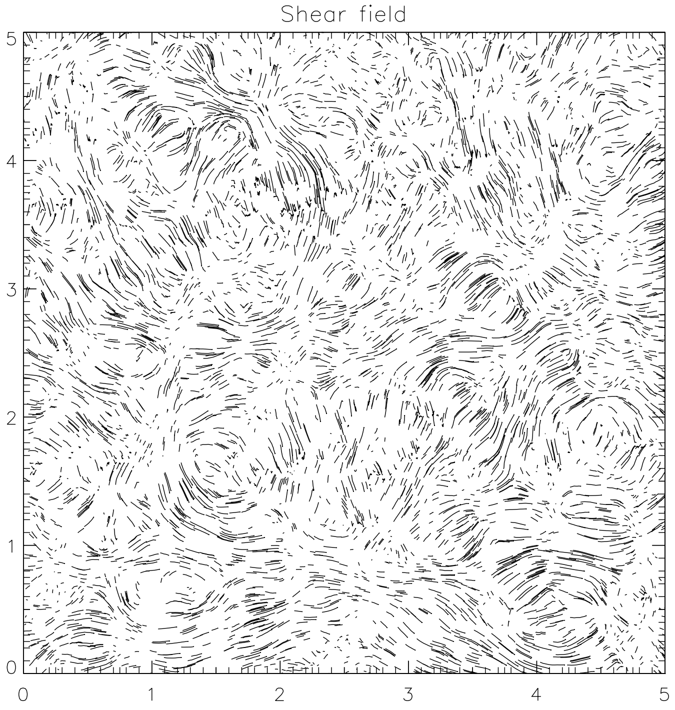

Fig. 3. Example of shear map obtained from a numerical simulation (open CDM model, for an 5 × 5 square degree survey, van Waerbeke et al. 1999).

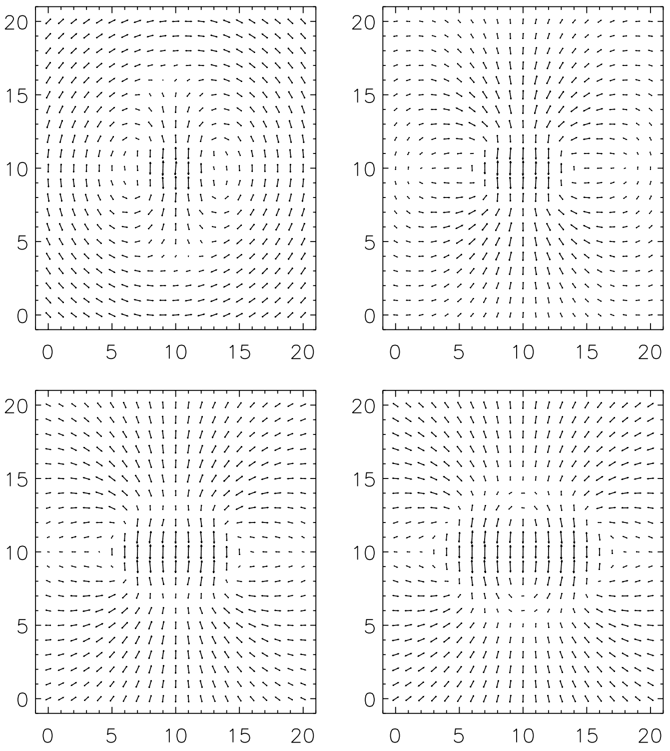

Fig. 4. The shear pattern of $\langle(\gamma(x_1).\gamma(x_2))\gamma(x')\rangle$ measured in ray-tracing simulations (Jain et al. 2000) for increasing pair separation $|x_2 - x_1|$. The separations are, from top to bottom and left to right, 2, 4, 6, and 8 in plot units (1 unit corresponds to about 10″). The pair points are along the horizontal axis.

are rather complicated. In particular the circular shape expected around the pair points (according to the results of Sect. 2.2.2) are observed only at very large distances (more that 5 times the pair separation). At separation comparable to the pair distance the patterns increase in complexity, with a substantial part of the area with no significant correlation. The most striking feature is the quasi-uniform shear orientation along the segment joining the two points. This effect, which is expressed in Eq. (35) where a uniform component is explicitly predicted, clearly strengthens between the pair points. Such a feature might appear somewhat surprising but a close inspection of synthetic shear maps (Fig. 3) indeed reveals many highly contrasted clumpy regions surrounded by strong coherent shear patterns primarily oriented transversely to directions between clumps.

The central pattern is the strongest and the most typical feature of the three-point correlation map and should be the easiest detectable one in the data. The previous analytical results suggest that such a structure is expected to hold for power law indices between −2 and −1 and should then be robust enough to be used as a detection tool of non-Gaussian regions. More detailed analysis performed along this idea are presented in the following.

3. Comparison with numerical simulations

The numerical simulations we use are described in Jain et al. (2000). The cosmological model is an open Universe ($\Omega_{\rm m} = 0.3$, $\Omega_\Lambda = 0$) with a Cold Dark Matter power spectrum ($\Gamma = 0.21$) and a normalization $\sigma_8 = 0.85$. The sources are located at redshift unity and the simulation area covers about 11 square degrees with a resolution of 0.1 arcmin.

The shear patterns for pair points at increasing separation are shown in Fig. 4. A visual inspection of their morphology and strength confirms that the uniform shear pattern within an ellipse that encompasses the pair points (as described in the next section) is likely an optimum way to extract a non-Gaussian signal. When the separation is small, the overall circular shear pattern is clearly visible. When the separation increases, the shear appears uniform in the neighborhood of the segment joining the pair points and is mostly radial at finite distance. We have already seen that these results might be somewhat dependent on the power spectrum index. For this simulation the index varies from −1.3 to −1 and it is thus natural that the patterns look like those obtained in the case of a power-law model $n = -1$.

4. Improved measurement strategies

In this section we compare the measurements made in mock catalogs that mimic a large number of observational effects with different input models. We use these results to develop different survey strategies adapted to real data sets.

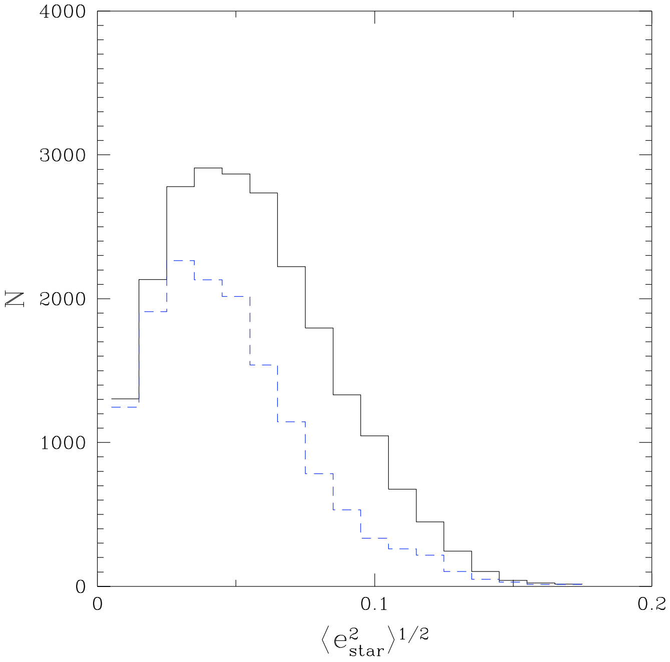

Fig. 5. Histogram of the Point Spread Function anisotropy of the stars in the simulated images (solid line) and in the VIRMOS-DESCART survey (dashed line).

4.1. Mock catalogues

The mock catalogues are generated from simulated sky images following the procedure described in Erben et al. (2001). The only difference here is that the galaxies are lensed according to a realistic cosmic shear signal, using ray-tracing simulations (Jain et al. 2000) instead of having a constant shear amplitude as in Erben et al. 2001. The galaxies are analyzed exactly in the same way as real data, following the procedure described in van Waerbeke et al. (2000, 2001b). In particular, the mock catalogues have the three main features encountered in the actual surveys:

- galaxy intrinsic shape fluctuations;
- masks;
- noise from galaxy shape measurements and systematics from PSF corrections,

and the simulated images reproduce observational conditions matching our data set (PSF anisotropy, limiting magnitude, luminosity functions, galaxy and star number densities, intrinsic ellipticity...). The PSF anisotropy is even larger than the one in our data set, as shown in Fig. 5, but it is uniform[6]. We used two ray-tracing simulations from Jain et al. (2000): one is OCDM, as described in Sect. 3, and the other is a τCDM with $\Gamma = 0.21$ and $\Omega_{\rm m} = 1$. For each simulation we produced 11 square degrees of simulated sky images containing roughly 30 galaxies per arcmin^2, with a pixel size of 0.2 arcsec. The galaxies are lensed following the ray-tracing shear before generating the image[7]. In addition to the galaxy mock catalogues, we produced a reference catalogue containing only the cosmic shear values. We can therefore study separately the effect of masks, the ellipticity Poisson noise, real noise and systematics, when compared to the reference catalogue results.

4.2. Detection strategy

The adopted strategy is to measure the two component quantity

$$\overline{\xi_3}(|\boldsymbol{x}_1-\boldsymbol{x}_2|) = \int_{\rm ellipse} \frac{{\rm d}^2\boldsymbol{x}'}{V_{\rm ellipse}} \langle(\boldsymbol{\gamma}(\boldsymbol{x}_1).\boldsymbol{\gamma}(\boldsymbol{x}_2))\ \boldsymbol{\gamma}(\boldsymbol{x}')\rangle \qquad (38)$$

for different separations. The *bar* means we perform the average of $\langle(\boldsymbol{\gamma}(\boldsymbol{x}_1).\boldsymbol{\gamma}(\boldsymbol{x}_2))\ \boldsymbol{\gamma}(\boldsymbol{x}')\rangle$ within the area defined by $V_{\rm ellipse}$. The ellipse properties are defined to cover an area that encompasses the pair points in which the orientation of the shear pattern is expected to be uniform. To be more specific, after some trials we have obtained a good balance between the signal intensity and the shot noise amplitude when the ellipse has a 0.4 eccentricity, the pair points being its foci (see in Fig. 2).

The computation time can be reduced by building first a Delaunay triangulation (Delaunay 1934; see also van de Weygaert 1991) of the survey so that the neighbor list of any galaxy in the survey can be easily (and quickly) constructed. The quantity $\overline{\xi_3}(|\boldsymbol{x}_1-\boldsymbol{x}_2|)$ is a pseudo-vector, but its second component, e.g. the one corresponding to elongation at 45 degrees to $\boldsymbol{x}_1-\boldsymbol{x}_2$, vanishes on average for symmetry reasons. Therefore we only have to compute one component, which we define as,

$$\overline{\xi}_3^{\rm t}(d_{ij}) = \frac{\sum_{ijk} w_i\, w_j\, w_k\, (\boldsymbol{e}_i.\boldsymbol{e}_j)\ e_k^{(ij)}}{\sum_{ijk} w_i\, w_j\, w_k} \qquad (39)$$

where $\boldsymbol{e}_i$ are the galaxy ellipticities, $e_k^{(ij)}$ is the tangential (e.g. first) component, with respect to the segment $\boldsymbol{x}_j-\boldsymbol{x}_i$, of the ellipticity of the galaxy of index k, w_i are weights associated with each galaxy. The sums are made under the following constraints:

- $d_{ik} > d_{\rm min}$, $d_{jk} > d_{\rm min}$ so that close pairs are excluded to avoid spurious small angular scale signals (van Waerbeke et al. 2000) and
- $d_{ik}+d_{jk} < 1.1\, d_{ij}$ so that galaxy k is within the previously defined ellipse and the sum is split in bins according to the d_{ij} distance.

We then plot the reduced three point function, that is $\overline{\xi}_3^{\rm t}$ in units of $[\xi_2(d_{ij})]^2$,

$$\xi_2(d_{ij}) = \frac{\sum_{ij} w_i\, w_j\, (\boldsymbol{e}_i.\boldsymbol{e}_j)}{\sum_{ijk} w_i\, w_j}. \qquad (40)$$

The noise is estimated by computing the r.m.s. of the estimator in small individual bins (for which the noise dominates the signal), and then rebinned in the final, larger, bins (as described in Pen et al. 2002). The noise of the reduced three-point function is computed assuming that the noise of the second and the

---

[6] However, we do NOT assume a uniform PSF for the PSF correction; as for the real data, we fit the PSF with a 2D second order polynomial.

[7] That is, the image of the galaxies is not lensed. We first lens the catalogue of source galaxies and then use it to generate the sky images.

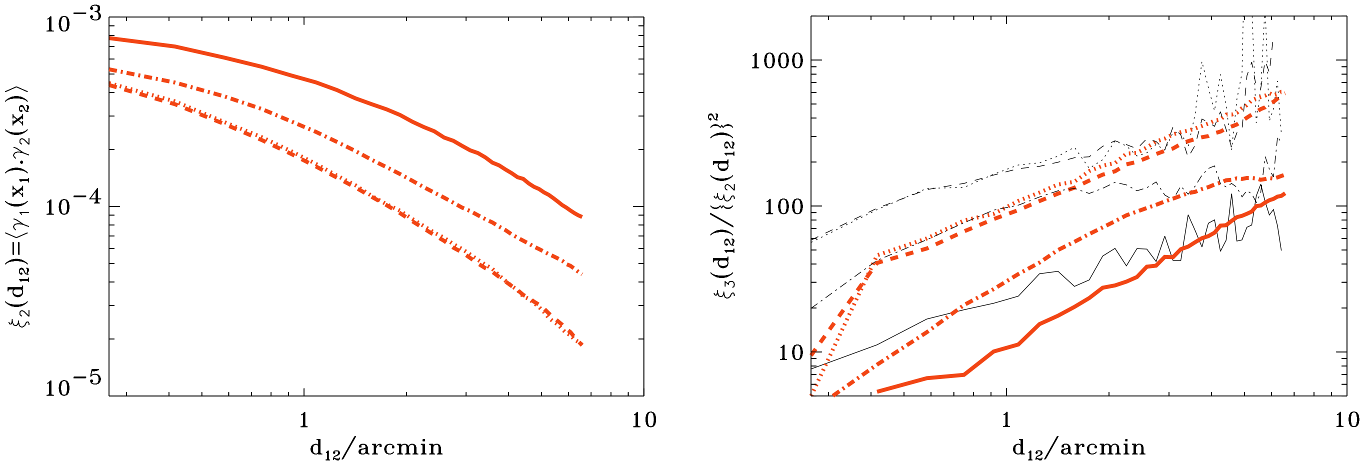

Fig. 6. Results for the measured value of the two-point function and the reduced three-point function (as defined in Eq. (38)) as a function of the pair distance for an Open CDM model (thick dashed lines) a ΛCDM (thick dot-dashed lines) and a τCDM model (thick solid lines). Results obtained in an Open CDM models with masks is shown as thick dotted lines. Galaxies in the catalogs have no intrinsic ellipticities. The measurements are made in bins of width 10″. The thin lines of the right panel corresponds to $200\,(n+2)/(-n)$, $150\,(n+2)/(-n)$ and $60\,(n+2)/(-n)$ for the open, Λ and τ CDM case respectively, where n is the power spectrum index measured from the slope of the corresponding two-point correlation functions.

third moments are uncorrelated. This might not be exact but the consequence of this assumption is insignificant since the main contribution to the noise of the ratio is in general the three-point moment.

4.3. Behavior of the reduced three-point function

In Fig. 6 we show the behavior of the reduced three-point function in the simulations. These simulations do not contain any noise, except that the shear field is measured in discrete randomly-placed points. It is found to be a slowly growing function of scale. This might first appear surprising (this ratio is expected to be constant for a constant Q) but this result should be examined in the light of Eq. (33) and the subsequent comments: at small scale n decreases, therefore it is expected that the reduced three-point function also decreases. Indeed, as demonstrated in the right panel of Fig. 6, the reduced ratio behaves approximately as $(n+2)/n$ at least for scales above 2′ with a multiplicative coefficient (200, 150 and 60 for respectively an open, Λ and τ CDM model) that roughly corresponds to the values of the convergence skewness s_3 at small scale in those models (Hui 1999).

On this plot the effects of masks on these quantities are shown as dotted lines. As expected, its effect on the two-point function is null. Its effect on the three-point function as measured here is not totally absent (different configurations taken into account in Eq. (38) may have different weights when masks are taking into account). It appears however that it has a negligible effect compared to the other sources of noise.

Figure 7 also shows the amplitude of the cosmic variance to be expected in an 11 square degree survey for the reduced three-point function and in the case of an Open CDM model (dotted dashed lines). These error bars have been obtained from the results obtained in 7 realizations of the same model. They show that a 30% fluctuation is to be expected in the signal. Note also that the error bars *are* correlated in the different bins.

4.4. Optimization and noise effects

A proper choice of weights w_i is essential to get a good signal to noise ratio. We have found that the introduction of a cut-off in the galaxy ellipticity distribution,

$$w_i \sim \exp\left(-\frac{e_i^2}{2\,e_0^2}\right), \tag{41}$$

improves the signal detection but may also affect its amplitude. In Fig. 7 a cut-off is introduced with $e_0 = 0.5$ in order to improve the S/N ratio. If the measured shear is simply the sum of the intrinsic shear and some noise,

$$\boldsymbol{e}_i = \boldsymbol{\gamma}(\boldsymbol{x}_i) + \epsilon_i \tag{42}$$

then the cut in e translates to a cut in γ that can be simply described. The result depends on the shape of the intrinsic ellipticity PDF, $P(\epsilon)$,

$$\boldsymbol{\gamma}_i^{\rm cut} = \frac{\int {\rm d}^2\boldsymbol{\epsilon}\,(\boldsymbol{\gamma}(\boldsymbol{x}_i)+\epsilon_i)\,P(\epsilon)\,\exp\left(-\frac{(\gamma_i+\epsilon)^2}{2\,e_0^2}\right)}{\int {\rm d}^2\boldsymbol{\epsilon}\,P(\epsilon)\,\exp\left(-\frac{(\gamma_i+\epsilon)^2}{2\,e_0^2}\right)}. \tag{43}$$

If the cut-off value e_0 is large enough compared to the typical excursion of cosmic shear values, then this equation can be linearized in γ and one finds that

$$\boldsymbol{\gamma}_i^{\rm cut} = f_{\rm c}\,\boldsymbol{\gamma}(\boldsymbol{x}_i) + \dots \tag{44}$$

with

$$f_{\rm c} = \frac{\int \epsilon\,{\rm d}\epsilon\left(1-\frac{\epsilon^2}{2\,e_0^2}\right)\,P(\epsilon)\,\exp\left(-\frac{\epsilon^2}{2\,e_0^2}\right)}{\int \epsilon\,{\rm d}\epsilon\,P(\epsilon)\,\exp\left(-\frac{\epsilon^2}{2\,e_0^2}\right)}. \tag{45}$$

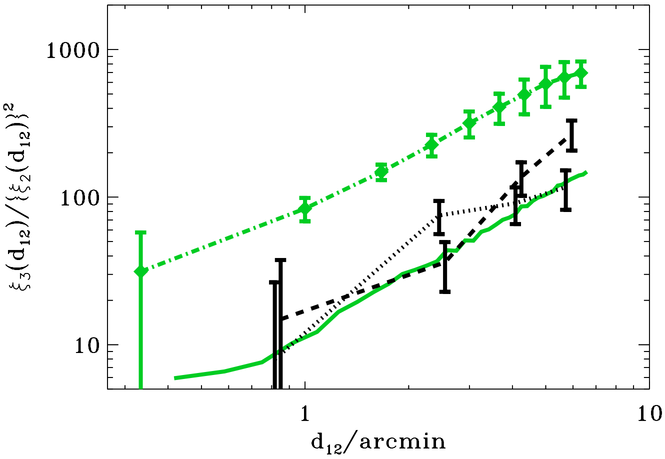

Fig. 7. The reduced three-point function as in the previous figure for different noise types in the catalogs. Error-bars for the open CDM model (dotted-dashed line) correspond to a *cosmic variance* estimation. The plot also compares the case of exact ellipticities for a τCDM model (solid lines) with the case where galaxies have intrinsic ellipticities (dotted lines, the measurement is made in 4 independent bins) and the case where noise in the shape determination are included (after PSF corrections, etc., dashed lines, 4 bins). Error bars correspond here to *measurement errors*, not to the cosmic variance, and are therefore uncorrelated.

For the adopted ellipticity distribution and for $e_0 = 0.5$, the value of f_c is about 0.8. Moreover the cut-off is large enough to have no impact on the non-Gaussian properties of the shear field (e.g. sub leading order terms in Eq. (44) have a negligible effect).

These numerical investigations are useful for exploring the effects of various types of noise. As expected the intrinsic ellipticities increase the noise, but do not bias the result. For 11 square-degrees surveys the signal to noise for the detection in a τCDM model is still comfortable (see Fig. 7). Masking effects are also rather mild. They bias very weakly the results (see Fig. 6) and only slightly deteriorate the signal to noise ratio when intrinsic ellipticities are taken into account (because the number of available pairs or triplets is smaller).

Moreover, when similar measurements are made in mock catalogues that incorporate realistic noise we described above, we recover the expected signal with a still reasonable signal to noise ratio: it is still larger than 3 in 3 independent bins (see Fig. 7). Note that the S/N ratio for the reduced skewness is not only sensitive to the amplitude of the three point function, but also to the amplitude of the 2-point function. On the lower curves of Fig. 7, only the noise coming from the three-point function measurement is shown. Its amplitude is roughly independent of the cosmological model (it scales basically as the inverse square root of the number of triplets available).

5. Conclusion

We have presented various geometrical patterns that the shear three-point correlation function is expected to exhibit. Its dependence on the cosmological parameters is found to be similar to that of the skewness of the convergence field, opening an alternative way to break the degeneracy between the amplitude of the density fluctuations, σ_8, and the density parameter of the Universe Ω_m. However, the reduced three-point function of the shear is more dependent on the power spectrum index than the skewness. In particular it is expected to vanish when the index gets close to −2. Numerical investigations have nonetheless proved the shear patterns to be robust enough to provide a solid ground for the detection of non-Gaussian properties in cosmic shear fields.

We proposed a detection strategy that has been tested in mock catalogues that include realistic noise structures such as residual systematics and PSF anisotropy as seen in the real data. The quality of the PSF correction is always good enough to provide an accurate measurement of the shear three-point function. Since the mock catalogues were designed to reproduce the characteristics of the current VIRMOS-DESCART lensing survey, we conclude that non-Gaussian signals should be detectable in this data set. The results of our investigations are presented in another paper (Bernardeau et al. 2002).

Beyond the detection, the scientific exploitation of the 3-point function for cosmology also depends on our ability to overcome other important difficulties. For instance, we found the cosmic variance amplitude to be of the order of 30% of the signal of the reduced three-point function, in agreement with previous studies made for the convergence. Other issues regarding source clustering, source redshift uncertainties, and intrinsic alignment of galaxies have not been considered here.

The measurement of non-Gaussian signatures in lensing surveys is of course of great interest because it provides an independent measure of the mean mass density of the Universe in addition to testing the gravitational instability paradigm which leads to large-scale structures. It is likely that the analysis of cosmological non-Gaussian signatures will be one of the major and most promising goals of emerging dedicated lensing surveys[8] that take advantage of panoramic CCD cameras of the MEGACAM generation (Boulade et al. 2000).

Acknowledgements. We thank B. Jain for providing his ray-tracing simulations, and the referee P. Schneider for a very useful and detailed report. This work was supported by the TMR Network "Gravitational Lensing: New Constraints on Cosmology and the Distribution of Dark Matter" of the EC under contract No. ERBFMRX-CT97-0172. The numerical calculations were partly carried out on MAGIQUE (SGI-O2K) at IAP. The simulated sky images used in this work are available upon request (60Gb). FB thanks IAP for hospitality.

References

Bacon, D. J., Refregier, A. R., & Ellis, R. S. 2000, MNRAS, 318, 625
Benabed, K., & Bernardeau, F. 2001, PRD, 64, 3501B
Bernardeau, F. 1995, A&A, 301, 309
Bernardeau, F. 1996, A&A, 312, 11
Bernardeau, F., van Waerbeke, L., & Mellier, Y. 1997, A&A, 322, 1
Bernardeau F., Mellier, Y., & van Waerbeke, L. 2002, A&A, 389, L28
Bernardeau, F., Colombi, S., Gaztanaga, E., & Scoccimarro, R. 2001, Phys. Rep., in press [`astro-ph/0112551`]

---

[8] Such as the Canada-France-Hawaii Telescope Legacy Survey, `http://www.cfht.hawaii.edu/Science/CFHLS/`

Bernardeau, F., & Valageas, P. 2000, A&A, 364, 1

Boulade, O., Charlot, X., Abbon, P., et al. 2000, SPIE, 4008, 657

Colombi, S., Bernardeau, F., Bouchet, F. R., & Hernquist, L. 1997, MNRAS, 287, 241

Delaunay, B. N. 1934, Bull. Acad. Sci. USSR: Classe Sci. Mat., 7, 793

Erben, T., van Waerbeke, L., Bertin, E., Mellier, Y., & Schneider, P. 2001, A&A, 366, 717

Hui, L. 1999, ApJ, 519, L9

Jain, B., & Seljak, U. 1997, ApJ, 484, 560

Jain, B., Seljak, U., & White S. 2000, ApJ, 530, 547

Kaiser, N. 1992, ApJ, 388, 272

Kaiser, N. 1998, ApJ, 498, 26

Kaiser, N., Squires, G., Fahlman, G., & Woods, D. 1994, in Clusters of galaxies, ed. F. Durret, A. Mazure, & J. Tran Thanh Van (Éditions Frontières)

Kaiser, N., Wilson, G., & Luppino, G. 2000 [`astro-ph/0003338`]

Limber, D. 1954, ApJ, 119, 655

Maoli, R., et al. 2001, A&A, 368, 766

Pen, U.-L., van Waerbeke, L., & Mellier, Y. 2002, ApJ, 567, 31

Schneider, P. 1996, MNRAS, 283, 837

Schneider, P., van Waerbeke, L., Jain, B., & Kruse, G. 1998, MNRAS, 296, 873

Scoccimarro, R., & Frieman, J. A. 1999, ApJ, 520, 35

Scoccimarro, R., & Couchman, H. 2001, MNRAS, 325, 1312

Stebbins, A. 1996 [`astro-ph/9609149`]

Tóth, G., Hollósi, J., & Szalay, A. S. 1989, ApJ, 344, 75

van de Weygaert, R. 1991, Ph.D. Thesis, Leiden University

van Waerbeke, L., Bernardeau, F., & Mellier, Y. 1999, A&A, 342, 15

van Waerbeke, L., Mellier, Y., Erben, T., et al. 2000, A&A, 358, 30

van Waerbeke, L., Hamana, T., Scoccimarro, R., Colombi, S., & Bernardeau, F. 2001a, MNRAS, 322, 918

van Waerbeke, L., Mellier, Y., Radovich, M., et al. 2001b, A&A, 374, 757

Villumsen, J. V. 1996, MNRAS, 281, 369

Wittman, D. H., Tyson, J. A., Kirkman, D., Dell'Antonio, I., & Bernstein, D. 2000, Nature, 405, 143